Received June 1999
Revised June 2000
Accepted June 2000

Heat transfer study of high speed flow over a spiked blunt body

R.C. Mehta
Aerodynamics Division, Vikram Sarabhai Space Centre, Trivandrum, India

Keywords *Flow, Heat transfer, High speed, Flux*

Abstract *Unsteady compressible, axisymmetric Navier-Stokes equations are solved for a flow over a forward facing spike attached to a heat shield for a freestream Mach number range of 1.3-4.5. A numerical simulation is carried out using a finite-volume discretization technique in conjunction with a multistage Runge-Kutta time-stepping scheme. Comparisons have been made with experimental results such as surface oil flow visualisation, schlieren picture and surface pressure distribution. A good agreement is found between them. Computed results show that lengths of the separated region on the spike are influenced by freestream Mach number. The interaction between the shear layer on the spike and the conical-reattachment shock wave causes the peak wall pressure and heat flux on the heat shield. The peak heat flux is shown to be a function of freestream Mach number and increases with increase in freestream Mach number.*

Nomenclature

Cf	= surface skin friction coefficient	U	= mean streamwise velocity
C_p	= specific heat at constant pressure, J/kg.K	u, v	= velocity components
		W	= conservative variables in vector form
Cp	= static pressure coefficient		
D	= payload shroud diameter, m	x, r	= coordinate directions, m
e	= specific energy, J/Kg		
F, G	= inviscid flux vector	*Greek symbols*	
H	= source vector	μ	= molecular viscosity, kg/m.s
M	= Mach number	ρ	= density, kg/m^3
p	= static pressure, N/m^2	σ_{rr}, σ_{xx}	= normal stress tensor, N/m^2
Pr	= Prandtl number	τ_{xr}	= shear stress tensor, N/m^2
q	= heat flux, W/m^2		
Re	= Reynolds number	*Subscripts*	
R, S	= viscous flux vector	w	= wall
t	= time, s	∞	= free stream condition

Introduction

High speed vehicles are designed to withstand severe aerodynamic heating conditions. Such vehicles include hypervelocity projectiles, re-entry vehicles and hypersonic aircraft. Maximum heating and the consequent potential for material erosion are a typical problem associated with the nose-region of the blunt body. In the flight regime 2-4km/s, the nose-region of the heat shield experiences significant heating and material erosion, causing unacceptable perturbations in the aerodynamic characteristics and the flight path. As an example of the severity of the heating, the stagnation temperature at sea level

International Journal of Numerical Methods for Heat & Fluid Flow, Vol. 10 No. 7, 2000, pp. 750-769.

and at a velocity of about 3.1km/s, i.e. at about Mach number 8.9, corresponds to the melting point of tungsten. Therefore, it is important to develop active or passive techniques to reduce the heating rates in the vicinity of the nose-region of the heat shield. Heat flux on the heat shield at high speed can be reduced by attaching a forward facing spike to the blunt body. But the conical shock of the spike impinges on the blunt region of the heat shield which may cause severe local heating. Therefore, the peak wall heat flux has to be calculated for the satisfactory performance of the thermal protection system. The spiked blunt body also reduces the aerodynamic drag at supersonic speeds.

Flow fields around spiked blunt bodies were experimentally investigated in the 1950s. These studies were concentrated on issues pertaining to high pressure and heating rates around such models and the mechanisms to minimize them. Stalder and Nielsen (1954) have carried out experiments on a hemisphere-cylinder configuration at freestream Mach numbers of 1.75, 2.67 and 5.04, and a Reynolds number range of 0.16×10^6 to 0.85×10^6 (based on the cylinder diameter). Their experimental studies reveal that the presence of a separated region over the spiked blunt body causes a detrimental increase in the heat transfer. Bogdonoff and Vas (1958) have observed experimentally that, for the spiked configuration, the heat transfer is less than half of the blunt body value at hypersonic Mach number. The heat transfer across the separated laminar boundary layer is reduced to about 56 per cent of the attached laminar boundary layer as predicted in a theoretical analysis of Chapman (1956). Crawford (1959) has investigated experimentally the effect of the spike length on the shape and nature of the flow boundaries, the pressure distribution, and the aerodynamic heating over the model surface at a freestream Mach number of 6.8 and a freestream Reynolds number of 0.12×10^6 to 1.5×10^6 based on the hemisphere cylinder diameter. According to their results, the aerodynamic drag and the heat flux are reduced when the spike is made longer, but the drag is not influenced further by the spike length when the latter exceeds roughly four times the blunt body diameter. Shang and Hankey (1980) have simulated flow field for a hemispherical nose spike of diameter 12.7mm attached to a truncated conical after-body of diameter 50.8mm, the semi-cone angle being about 9 degrees, at freestream Mach number of 3.0. Calarese and Hankey (1985) have tested and analysed the flow oscillations in the spiked-tipped model. Karlovskii and Sakharov (1986) have computed the flow over an axisymmetric frustrum of cone with protruding spherically blunted cylindrical spike of different lengths at supersonic speeds. Yamauchi *et al.* (1993) have recently investigated the flow field around a spiked blunt body at supersonic Mach numbers numerically. The focus of their numerical analysis was to investigate the mechanism of drag reduction and the pattern of flow field at different Mach numbers.

These experimental and numerical studies have given an insight into the characteristics of separated region created by adverse pressure gradients caused by conical shock interaction with the reattachment shock on the blunt body. The pressure rise at the start of separation, the shape of the boundary of

separation, and the pressure under the separated boundary are affected by the freestream Mach number and Reynolds number. To the author's best knowledge, a numerical analysis of heat transfer to the forward facing spike attached to a heat shield has not been reported in the open literature at high speeds, although computation of wall heat flux is an important quantity for designing the thermal protection system. Therefore, this is one of the objectives of the present numerical simulations, i.e. to study the peak pressure, the heat flux and the separation length at various supersonic Mach numbers. Axisymmetric, compressible Navier-Stokes equations are solved to obtain the flow field over a typical spiked heat shield configuration. The effect of interaction of the bow shock with the reattachment shock wave on the heat transfer is studied for the freestream Mach number range of 1.3-4.5.

Governing equations

Experimental data obtained from the wind-tunnel tests at zero angle of incidence show that the flow pattern remains the same with reference to the tunnel configuration even when the model is rotated. Measurements made at two diametrically opposite locations indicate that the flow is axisymmetric. Therefore, a numerical simulation of the axisymmetric compressible Navier-Stokes equations is attempted in order to understand the basic fluid dynamics and heat transfer over the forward facing spike attached to the heat shield. The governing equations can be written in the following strong conservation form

$$\frac{\partial \mathbf{W}}{\partial t} + \frac{\partial \mathbf{F}}{\partial x} + \frac{\partial \mathbf{G}}{\partial r} + \mathbf{H} = \left[\frac{\partial \mathbf{R}}{\partial x} + \frac{\partial \mathbf{S}}{\partial r}\right] \tag{1}$$

where

$$\mathbf{W} = r\begin{bmatrix} \rho \\ \rho u \\ \rho v \\ \rho e \end{bmatrix}, \quad \mathbf{F} = r\begin{bmatrix} \rho u \\ \rho u^2 + p \\ \rho uv \\ (\rho e + p)u \end{bmatrix}, \quad \mathbf{G} = r\begin{bmatrix} \rho v \\ \rho uv \\ \rho v^2 + p \\ (\rho e + p)v \end{bmatrix}$$

are the state and inviscid flux vectors. The viscous flux vectors are

$$\mathbf{R} = r\begin{bmatrix} 0 \\ \sigma_{xx} \\ \tau_{xr} \\ u\sigma_{xx} + v\tau_{xr} + q_x \end{bmatrix}, \quad \mathbf{S} = r\begin{bmatrix} 0 \\ \tau_{xr} \\ \sigma_{rr} \\ u\tau_{xr} + v\sigma_{rr} + q_r \end{bmatrix}, \quad \mathbf{H} = \begin{bmatrix} 0 \\ 0 \\ \sigma_{+} \\ 0 \end{bmatrix}$$

where q_x and q_r are components of the heat flux vector. Thus the viscous terms in the above equations become

$$\sigma_{xx} = -\frac{1}{2}\mu\nabla.U + 2\mu\frac{\partial u}{\partial x}$$

$$\sigma_{rr} = -\frac{2}{3}\mu\nabla.U + 2\mu\frac{\partial v}{\partial r}$$

$$\tau_{xr} = \tau_{rx} = \mu\left(\frac{\partial u}{\partial r} + \frac{\partial v}{\partial x}\right)$$

$$\sigma_{+} = -p - \frac{2}{3}\mu\nabla.U + 2\mu\frac{v}{r}$$

$$\nabla.U = \frac{\partial u}{\partial x} + \frac{\partial v}{\partial r} + \frac{v}{r}$$

$$q_x = -C_p\frac{\mu}{Pr}\frac{\partial T}{\partial x}$$

$$q_r = -C_p\frac{\mu}{Pr}\frac{\partial T}{\partial r}$$

where Pr is assumed to take a constant value of 0.72. The flow is assumed to be laminar as reported in Crawford (1959; Yamauchi *et al.* (1993); Priyadarshi *et al.* (1994). The coefficient of molecular viscosity is calculated according to Sutherland's formula. The temperature is related to pressure and density by the perfect gas equation of state as

$$p = (\gamma - 1)[e - \frac{1}{2}\rho(u^2 + v^2)] \tag{2}$$

The ratio of the specific heats was assumed constant and equal to 1.4.

Numerical scheme

Spatial discretization

To facilitate the spatial discretization in the numerical scheme, the governing fluid dynamics equation (1) can be written in the integral form over a finite volume as

$$\frac{\partial}{\partial t}\int_{\Omega}\mathbf{W}d\Omega + \int_{\Gamma}(\mathbf{F}dr - \mathbf{G}dx) = \int_{\Gamma}(\mathbf{R}dr - \mathbf{S}dx) - \int_{\Omega}\mathbf{H}d\Omega \tag{3}$$

where Ω is the computational domain, Γ is the boundary of the domain. The contour integration around the boundary of the cell is taken in the anti-clockwise sense.

The computational domain is divided into a finite number of non-overlapping quadrilateral cells. Figure 1 depicts a typical cell which has four edges (1, 2, 3, 4) and four vertices (A, B, C, D). The conservation variables within the computational cell are represented by their average values at the cell centre. When the integral governing equations (3) are applied separately to each cell in the computational domain, we obtain a set of coupled ordinary differential equations of the form

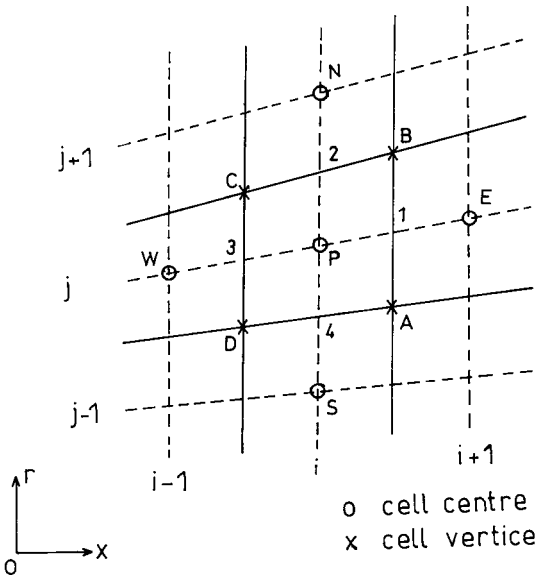

Figure 1.
Computational cell

$$A_{i,j}\frac{\partial \mathbf{W}_{i,j}}{\partial t} + Q(\mathbf{W}_{i,j}) - V(\mathbf{W}_{i,j}) + D(\mathbf{W}_{i,j}) + A_{i,j}(\mathbf{H}_{i,j}) = 0 \qquad (4)$$

where $A_{i,j}$ is the area of the computational cell, $Q(\mathbf{W}_{i,j})$ and $V(\mathbf{W}_{i,j})$ are the inviscid and viscous fluxes respectively, and $D(\mathbf{W}_{i,j})$ is the artificial dissipation flux added for numerical stability.

Inviscid terms

The convective fluxes are calculated at the centre, resulting in cell-centre flux balances. The contour integration of the inviscid flux vector is approximated as

$$Q(\mathbf{W}_{i,j}) = \sum_{s=1}^{4}(\mathbf{F}_s \Delta r_s - \mathbf{G}_s \Delta x_s) \qquad (5)$$

where s is the side of the computational cell. The summation is done over the four edges of the cell as depicted in Figure 1.

Viscous terms

The viscous terms are defined at the centre of the cell. The above procedure is repeated to approximate the contour integration of the viscous flux vector as

$$V(\mathbf{W}_{i,j}) = \sum_{s=1}^{4}(\mathbf{R}_s \Delta r_s - \mathbf{S}_s \Delta x_s) \qquad (6)$$

The inclusion of diffusive transport terms (**R** and **S**) requires a choice of the locations at which the derivatives of the primitive variables (u, v, T) should be

integrated. The cell used for gradient calculations forms a second mesh that is shifted a half cell in the axial and radial directions in relation to the original computational mesh. The derivatives $\partial f/\partial x$ and $\partial f/\partial r$ at the cell vertices (A, B, C, D) can be determined by considering auxiliary cells surrounding each side as depicted in Figure 1, where f stands for any of the primitive variables. The viscous flux vectors **R** and **S** are approximated in such a way as to preserve cell conservations and maintain algorithm simplicity. The derivatives of primitive variables at the vertices of the cell are evaluated by discrete application of the divergence theorem (Peyret and Vivind, 1993) to the auxiliary cell as

$$\begin{aligned} A'_{AB}\frac{\partial f}{\partial x}|_{AB} &= [(f_E - f_P)\Delta r_{AB} + (f_B - f_A)\Delta r_{PE}] \\ A'_{BC}\frac{\partial f}{\partial x}|_{BC} &= [(f_B - f_C)\Delta r_{PN} + (f_N - f_P)\Delta r_{BC}] \\ A'_{CD}\frac{\partial f}{\partial x}|_{CD} &= [(f_P - f_W)\Delta r_{CD} + (f_C - f_D)\Delta r_{PW}] \\ A'_{DA}\frac{\partial f}{\partial x}|_{DA} &= [(f_A - f_D)\Delta r_{PS} + (f_P - f_S)\Delta r_{DA}] \end{aligned} \tag{7}$$

where A′ is the area of the secondary cell. In a similar way the derivative of f in the other coordinate can be written. The discretized solution to the governing equations results in a set of volume average state variables of mass, momentum, and energy which are in balance with their area-averaged values. The net convective flux is computed by summing the inviscid and viscous terms. On sufficiently smooth grids the above finite volume discretization is second-order accurate in space.

Artificial dissipation

In cell-centred spatial discretization schemes, such as the one described above which is non-dissipative, where numerical errors (truncation, round-off, etc.) are not damped in time, oscillations may be present in the steady state solution. In order to eliminate these oscillations, artificial dissipative terms are added to equation (4). The approach of Jameson *et al.* (1981) is adopted to construct the dissipative function $D_{i,j}$ consisting of a blend of second and fourth differences of the vector conserved variables $\mathbf{W}_{i,j}$. Fourth differences are added everywhere in the flow domain where the solution is smooth, but are switched off in the region of shock waves. A term involving second differences is then switched on to damp oscillations near shock waves. This switching is achieved by means of a shock sensor based on the local second differences of pressure.

Time-marching scheme

The spatial discretization described above reduces the governing flow equations to semidiscrete ordinary differential equations. The temporal integration of equation (4) is performed using an efficient multistage scheme (Jameson *et al.*, 1981). The following three-stage, time-stepping method is adopted for the present work (neglecting for clarity, the subscripts i and j):

$$\begin{aligned}
\mathbf{W}^{(0)} &= \mathbf{W}^{n} \\
\mathbf{W}^{(1)} &= \mathbf{W}^{n} - 0.6\Delta t(\mathbf{Res}^{(0)} - \mathbf{D}^{(0)}) \\
\mathbf{W}^{(2)} &= \mathbf{W}^{n} - 0.6\Delta t(\mathbf{Res}^{(1)} - \mathbf{D}^{(0)}) \\
\mathbf{W}^{(3)} &= \mathbf{W}^{n} - 1.0\Delta t(\mathbf{Res}^{(2)} - \mathbf{D}^{(0)}) \\
\mathbf{W}^{n+1} &= \mathbf{W}^{(3)}
\end{aligned} \tag{8}$$

where n is the current time level, n + 1 is the new time level, and residual **Res** is the sum of the inviscid and viscous fluxes. In order to minimize the computation time, the expensive evaluation of the dissipation term **D** is carried out only at the first intermediate stage (0) and then frozen for the subsequent stages. A conservative choice of the Courant-Friedrichs-Lewy number (1.4) was made to achieve a stable numerical solution. The three-stage Runge-Kutta time-stepping scheme has been proved to be third-order accurate in time for a linear system of one-dimensional equation (Jameson *et al.*, 1981; Alonse *et al.*, 1995). A local time stepping is used to achieve a steady-state solution.

Boundary conditions

No-slip boundary condition has been applied on the solid wall of the heat shield. The solid surface has been considered to be isothermal (T_w = 300K). At the wall, the pressure has been obtained from an extrapolation of the interior mesh point of pressure value in the direction normal to the surface, i.e. normal pressure gradient is set to zero. For the outflow supersonic boundary, the vector of conserved quantities is linearly extrapolated from the interior grid points of the computational domain and inflow quantities are taken as freestream values. On the line of symmetry, ahead of the forward facing probe, mirror image conditions are imposed on the flow variables, except the normal velocity component, which is set equal to zero.

Model and grid agreement

The aforementioned numerical procedure is employed to obtain the flowfield along a typical payload shroud. The maximum heat shield diameter is D. The boat-tail angle is 5 degrees measured clockwise from the axis with reference to the oncoming flow direction. For the blunt nosed cone, the inclination at the forebody junction is 20 degrees. These subscale dimensions, as depicted in Figure 2, are chosen after considering the blockage and compatibility condition with the model system support of wind tunnel.

In order to initiate the numerical simulation of flow along the heat shield, the physical space is disretized into non-uniform spaced grid points. These body-oriented grids are generated using a finite element method in conjunction with homotopy scheme (Shang, 1981). The heat shield space is defined by a number of grid points in cylindrical coordinate system. Using these surface points as the reference nodes, the normal coordinate is then described by exponentially stretched field points ($x_{i,j}$, $r_{i,j}$) extending outwards up to an outer computational

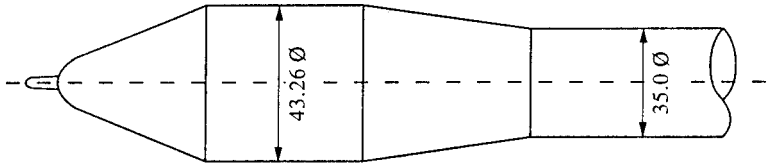

(a) Heat shield with spike

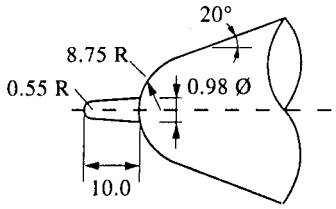

(b) A close-up view of spike

Figure 2.
The blunt body with forward facing spike

boundary. Sufficient grid points are allotted in the nose-cone and boat-tail regions. The stretching of grid points in the normal direction is obtained using the following expression:

$$x_{i,j} = x_{i,o}\left[\frac{e^{\frac{(j-1)\beta}{nr-1}}-1}{e^{\beta}-1}\right] + x_{i,w}\left[1-\frac{e^{\frac{(j-1)\beta}{nr-1}}-1}{e^{\beta}-1}\right]$$

$$r_{i,j} = r_{i,o}\left[\frac{e^{\frac{(j-1)\beta}{nr-1}}-1}{e^{\beta}-1}\right] + r_{i,w}\left[1-\frac{e^{\frac{(j-1)\beta}{nr-1}}-1}{e^{\beta}-1}\right] \qquad (9)$$

$$i = 1, 2, \ldots nx$$

$$j = 1, 2, \ldots nr$$

where $r_{i,w}$ and $r_{i,o}$ are wall and outer surface points, respectively, β is stretching factor, nx and nr are total number of grid points in x and r directions, respectively. These stretched grids are generated in an orderly manner. Grid independence tests are carried out, taking into consideration the effect of the computational domain, the stretching factor to control the grid intensity near the wall, and the number of grid points in the axial and normal directions. The outer boundary of the computational domain is varied from six to 15 times the payload shroud diameter. The blockage ratio (which is defined as the ratio of the maximum cross-sectional area of the model to the computational domain) is found to be in the range of 4-0.2 per cent. The grid stretching factor in the radial direction is varied from 1.5 to 5. The present numerical analysis is carried out on 132 $\times$ 62 grid points. The grid stretching factor is selected as 5, and the outer boundary of the computational domain is kept 15 times the payload

shroud diameter. The finer mesh near the wall helps to resolve the viscous effects. The coarse mesh helps in reducing the computer time. Figure 3 shows an enlarged view of the grid over the heat shield configuration. This grid arrangement is found to give a relative difference of about ±3 per cent in the pressure peak, which is in the same range as the pressure measurement error in the wind-tunnel with a blockage ratio of 0.3 per cent. The convergence criterion is based on the difference in density values at any grid point between two successive iterations, i.e. $|\rho^{n+1} - \rho^{n}| \leq 10^{-5}$.

Results and discussions

The current experimental data (Priyadarshi *et al.*, 1994) consist of schlieren pictures, the wall pressure distribution and surface oil flow pattern. The flow fields and their resulting wall pressure distributions are computed for freestream Mach number range of 1.3-4.5.

For the sake of brevity, zoomed view of vector plot for M_∞ of 1.5 and 2.0 over the spike is depicted in Figure 4. A strong recirculating flow at the spike region can be distinctly seen in the vector plots. The effect of Mach number over the flow separation can easily be observed. As the Mach number increases the dominance of the spike induced separation zone decreases. Re-attachment point moves aft on the nose fairing, and the separation angle becomes steeper with increasing freestream Mach number. It is important to mention here that the flow may become unsteady under certain conditions (Mair, 1952). The residual errors norms are found oscillating at some time level of iteration. This is attributed to the flow in the vicinity of the spike containing vorticity of the

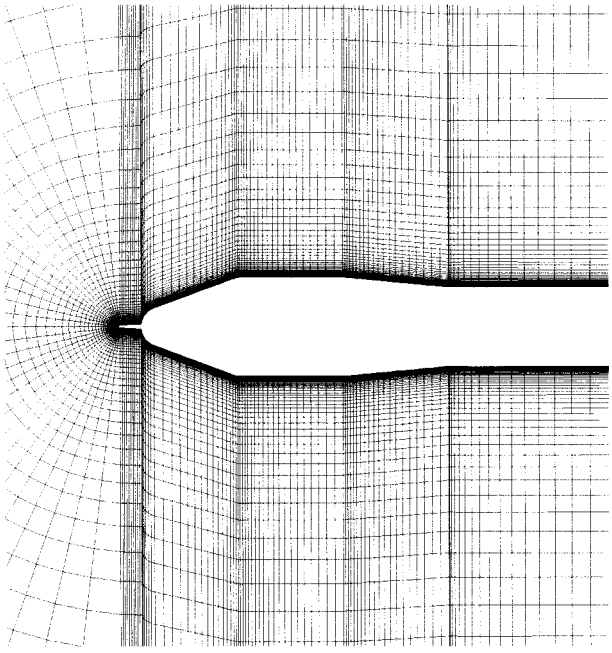

Figure 3.
Enlarged view of the computational grid

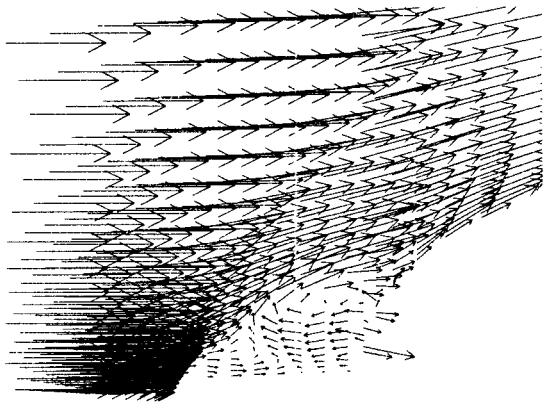

(a) $M_\infty = 1.5$

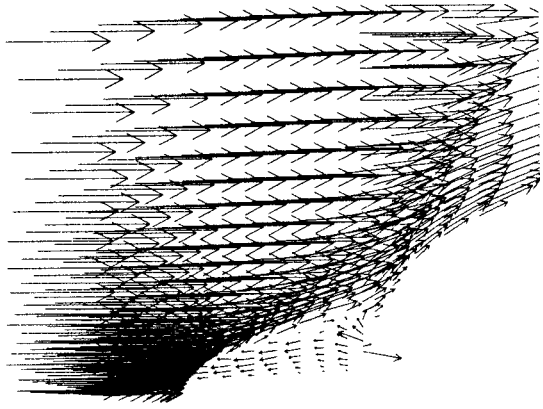

(b) $M_\infty = 2.0$

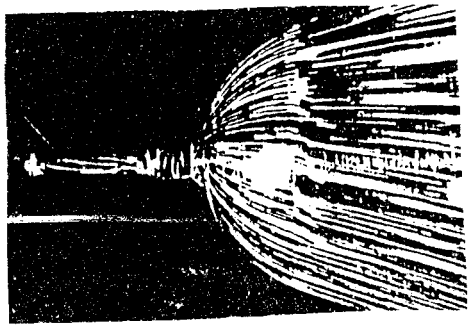

(c) $M_\infty = 2.0$

Figure 4.
Vector velocity plot and oil flow picture

separated region. Therefore, the strict steady-state solution cannot be achieved in the present numerical simulation. Since these computations do not have time accuracy on account of space variable time-stepping, we are unable to investigate the unsteadiness of the flow. Figure 4(c) presents the photograph of the surface flow patterns taken at $M_\infty = 2.0$ at zero angle of attack. At the base region of the spike, accumulations of oil followed by a relative oil free region is indicative of flow separation at the base region of the forward facing spike attached to the heat shield which also confirms the flow separation on the probe.

Figure 5 depicts the density contour plots in the vicinity of the spike. We can visualize from Figures 4(a), (b) and 5 the interaction between bow shock wave and re-attachment shock wave. The recirculation region behaves as if it has a spike boundary. The oil flow picture at $M_\infty = 2.0$ also shows the separated flow over the spiked-nose region which confirms the result of the numerical simulation.

To summarize the above flow field features, a schematic sketch of the flow field is illustrated in Figure 6 which is based on the observation of velocity vector and density contour plots near the spike region. The flow field is characterized by a formation of the conical shock wave in front of the spike, a separated flow region and interaction between the bow shock wave and the re-attachment shock wave. The separation region on the spike contributes to the reduction in dynamic pressure which is a function of freestream Mach number.

A complete flow field over the heat shield with spike and schlieren picture is presented in Figure 7 for $M_\infty = 1.5$, 1.7 and 2.0. The density contour plots show a complex flow field due to the presence of the spike. The schlieren pictures and density contour plots depict all the essential flow field features of the

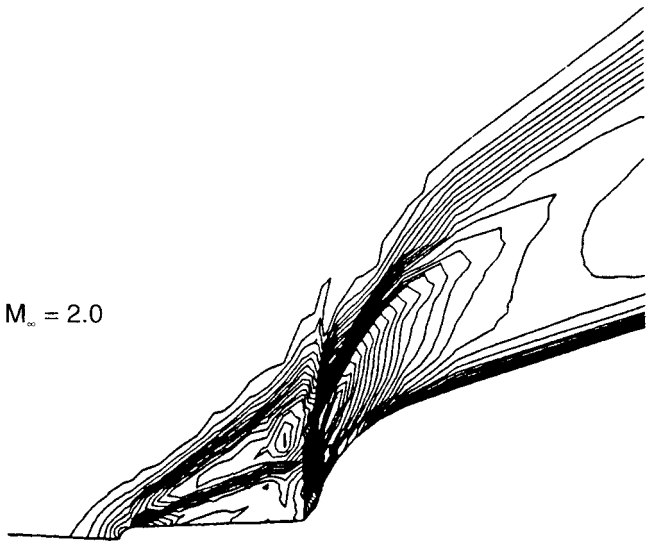

Figure 5.
Density contour plot in the spike region

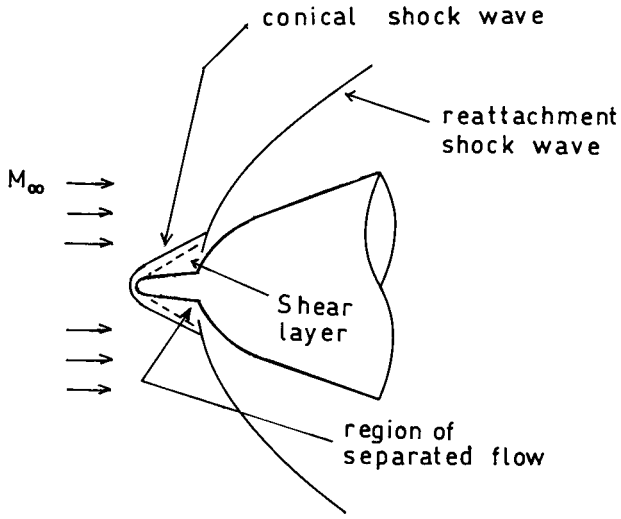

Figure 6.
Schematic sketch of the flow around spiked blunt body

supersonic flow such as formation of the bow shock over the spike, re-attachment shock and expansion fan over the shoulder of the heat shield for freestream Mach numbers of 1.5, 1.7 and 2.0.

Normal distance (Hoffmann and Chiang, 1994) from the wall is used in the computation of surface heat flux. Figures 8-13 depict the surface pressure distribution, skin friction coefficient and wall heat flux variation along the spiked blunt body surface for freestream Mach number range of 1.3-4.5. A very high pressure peak can be observed in the surface pressure coefficient distribution. The location of the pressure peak on the body is found at about x = 0.36m. This is the re-attachment point of the separated flow which does not vary with the freestream Mach number. The shear layer created on the spike region passes through the re-attachment shock wave and impacts on the blunt body surface, resulting in a pressure rise. A negative surface skin coefficient is found on the spike. It reveals a separated flow on the spike at all the freestream Mach numbers but the separation length is found to be dependent on the freestream Mach number. The wall heat flux shows a similar trend as the surface pressure coefficient distribution. The peak in the heat flux is found at about the same location as the pressure coefficient. The surface pressure coefficient shows good agreement with the experimental data (Priyadarshi *et al.*, 1994). The peak heat flux is observed at about x = 0.36m for all the freestream Mach numbers. The surface heat flux increases with increase in the freestream Mach number.

Conclusions

Numerical simulation over a forward facing spike attached to a blunt body is carried out for supersonic Mach numbers in the range of 1.3-4.5. Time dependent axisymmetric Navier-Stokes equations are solved to compute the flow field over the spike attached with the blunt body. A multistage Runge-

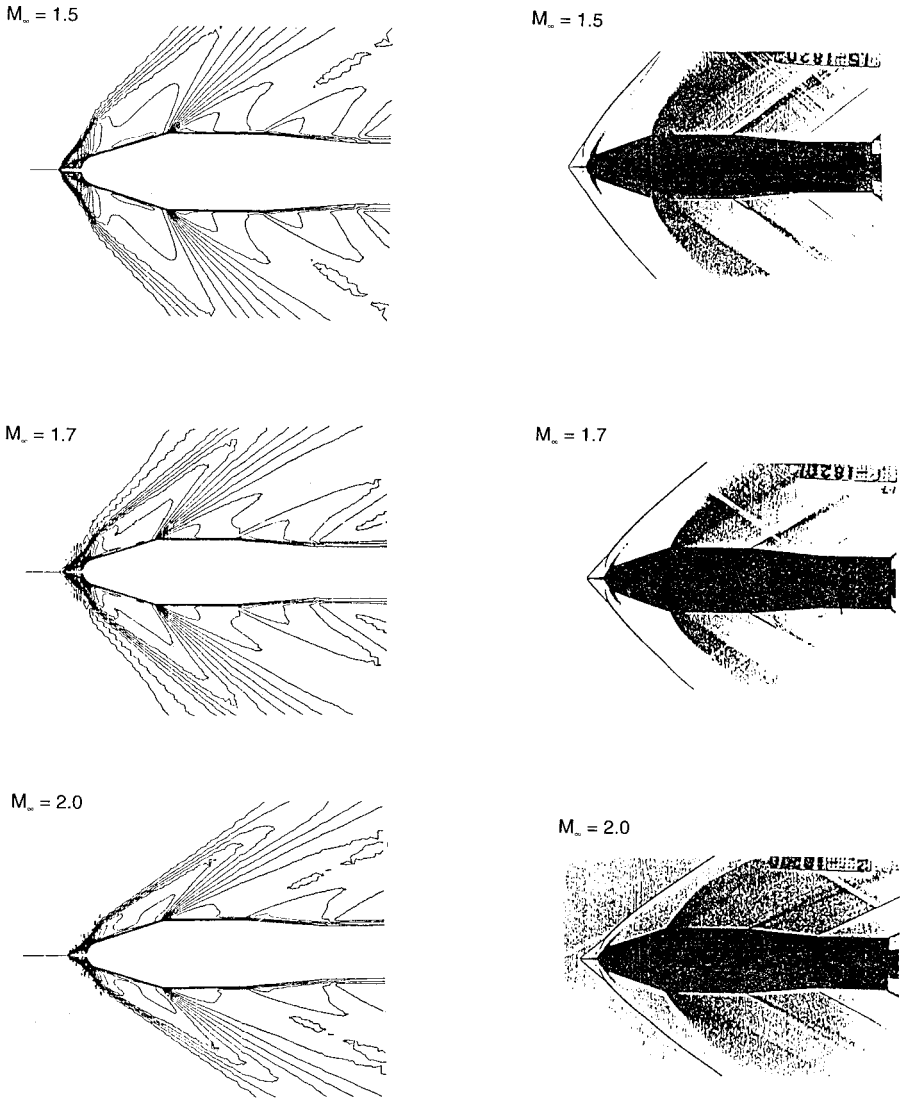

Figure 7.
Comparison between density contour and schlieren pictures

Kutta time stepping scheme is employed to get steady state solution. Numerical results are compared with the schlieren pictures, oil flow pattern and surface pressure distribution. The numerical results capture all the essential flow field features very well and show good agreement with the experimental data. The peak in the pressure and the heat flux is found on the blunt nose region at the same location for all the freestream Mach numbers. The shear layer created on the spike region passes through the re-attachment shock wave, which is influenced by the conical shock-re-attachment interaction, giving rise to the peak surface pressure and heat flux on the heat shield. Further extension of this work to three-dimensions is planned.

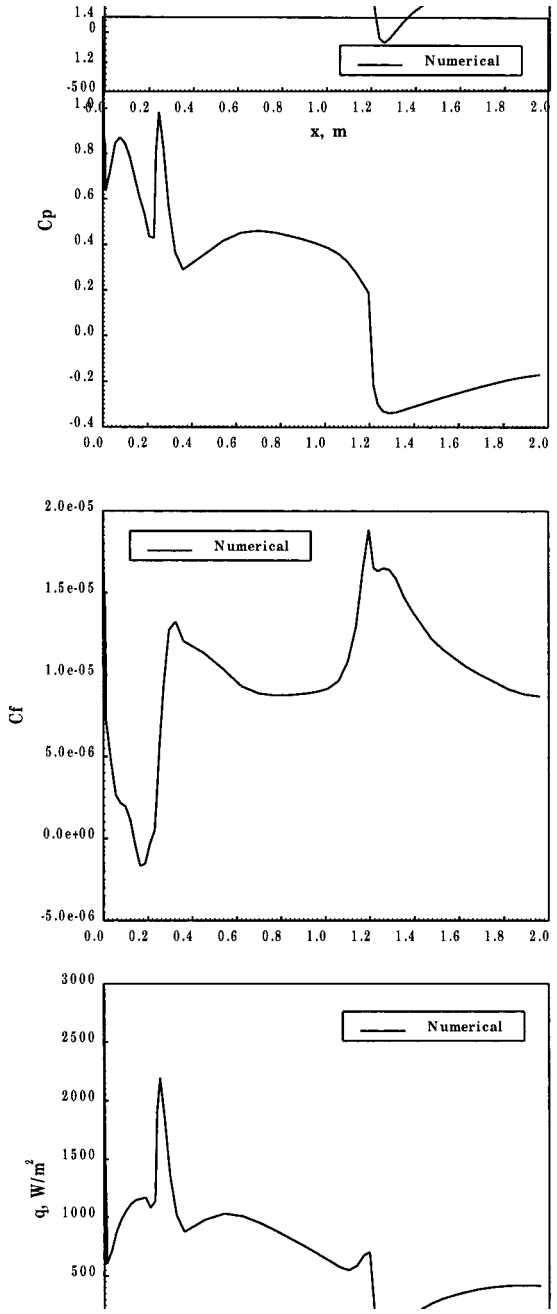

Figure 8.
Distribution of surface pressure coefficient, skin friction coefficient and wall heat flux at $M_\infty = 1.3$

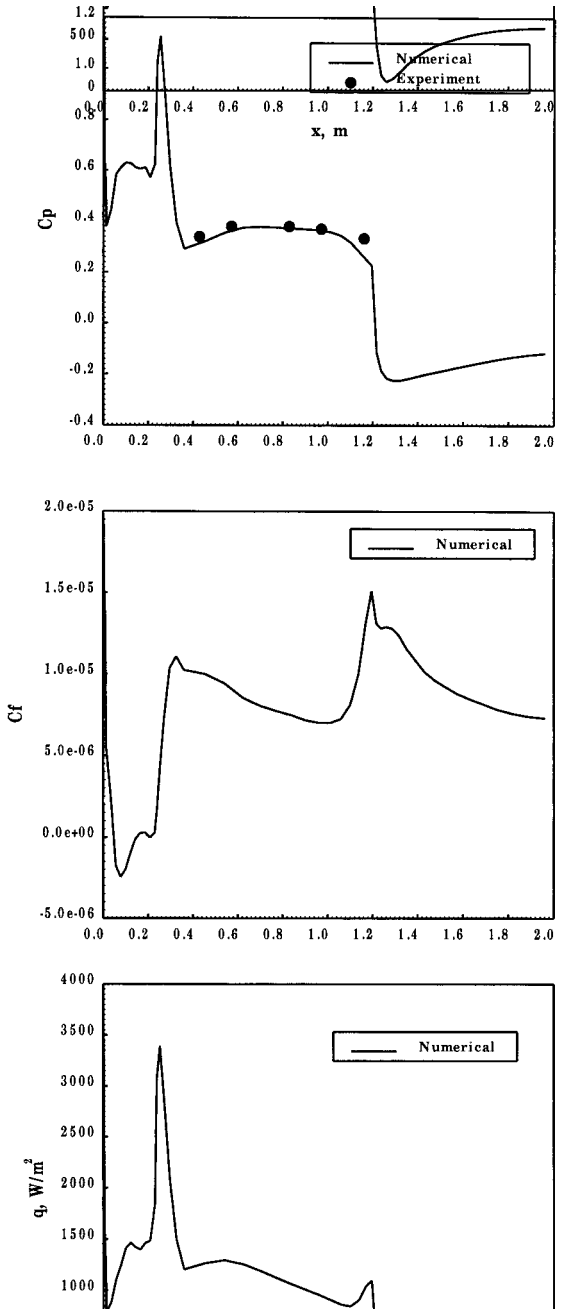

Figure 9.
Distribution of surface pressure coefficient, skin friction coefficient and wall heat flux at $M_\infty = 1.5$

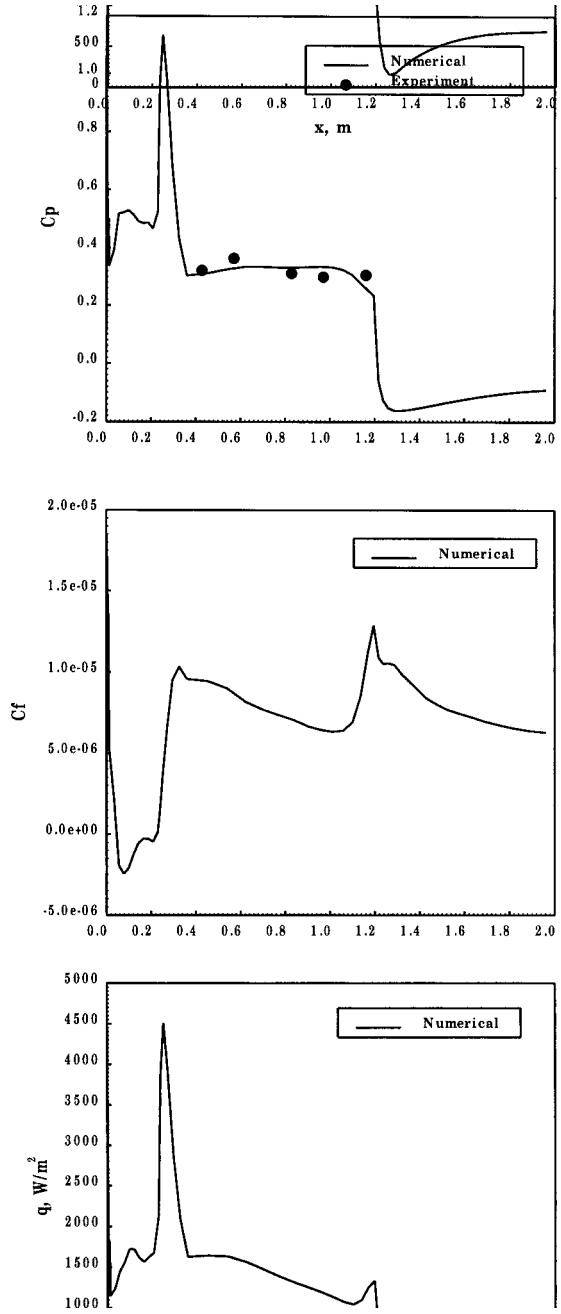

Figure 10.
Distribution of surface pressure coefficient, skin friction coefficient and wall heat flux at $M_\infty = 1.7$

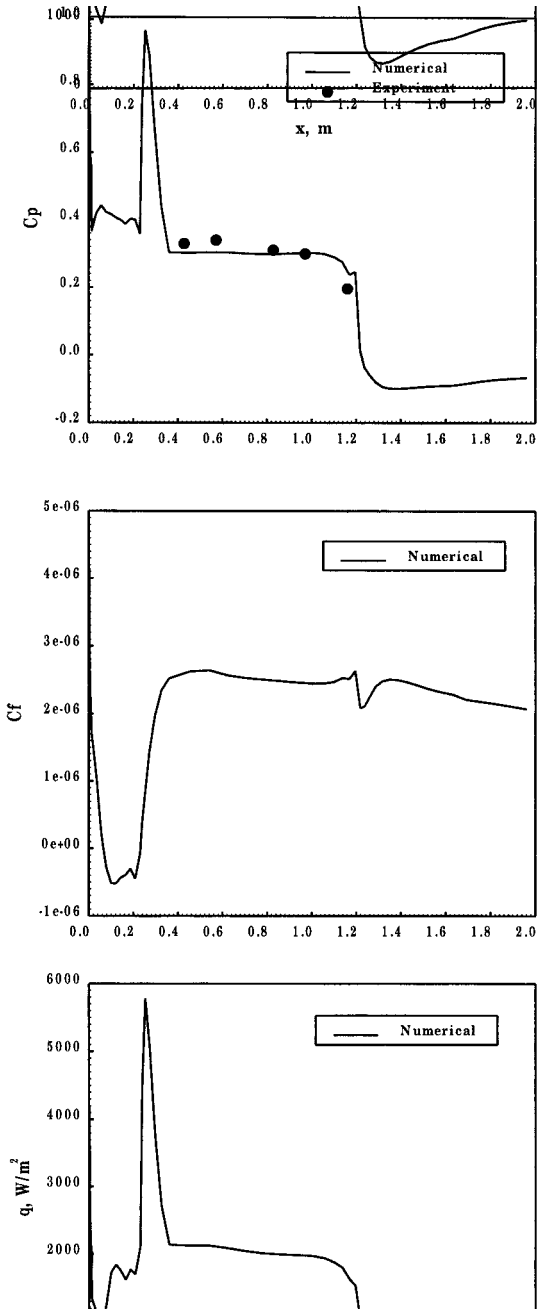

Figure 11.
Distribution of surface pressure coefficient, skin friction coefficient and wall heat flux at $M_\infty = 2.0$

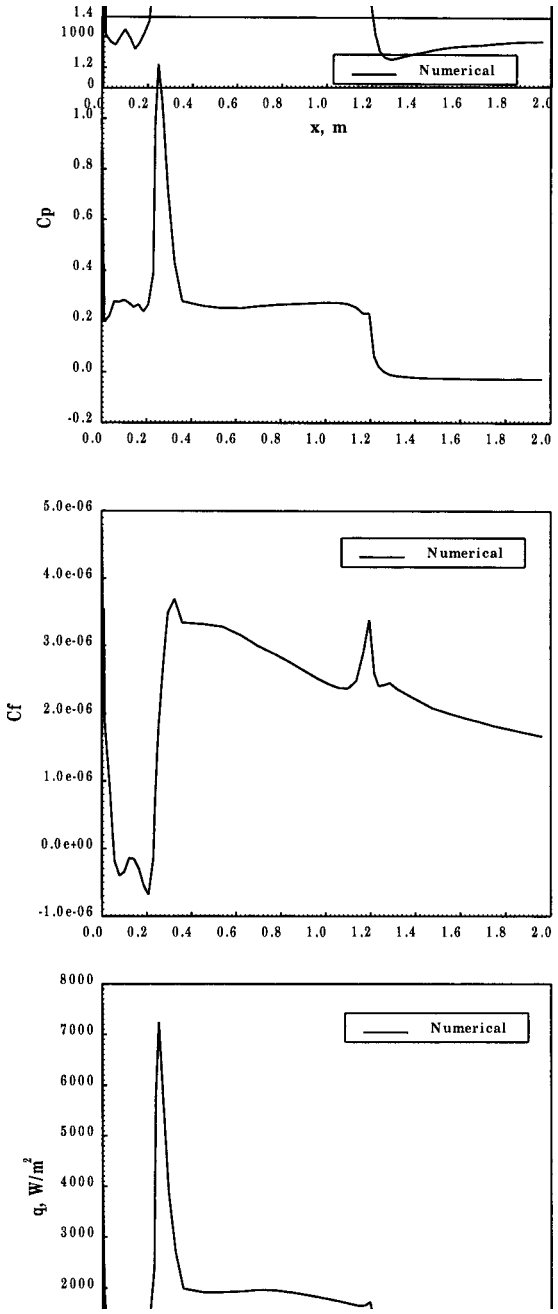

Figure 12.
Distribution of surface pressure coefficient, skin friction coefficient and wall heat flux at $M_\infty = 3.0$

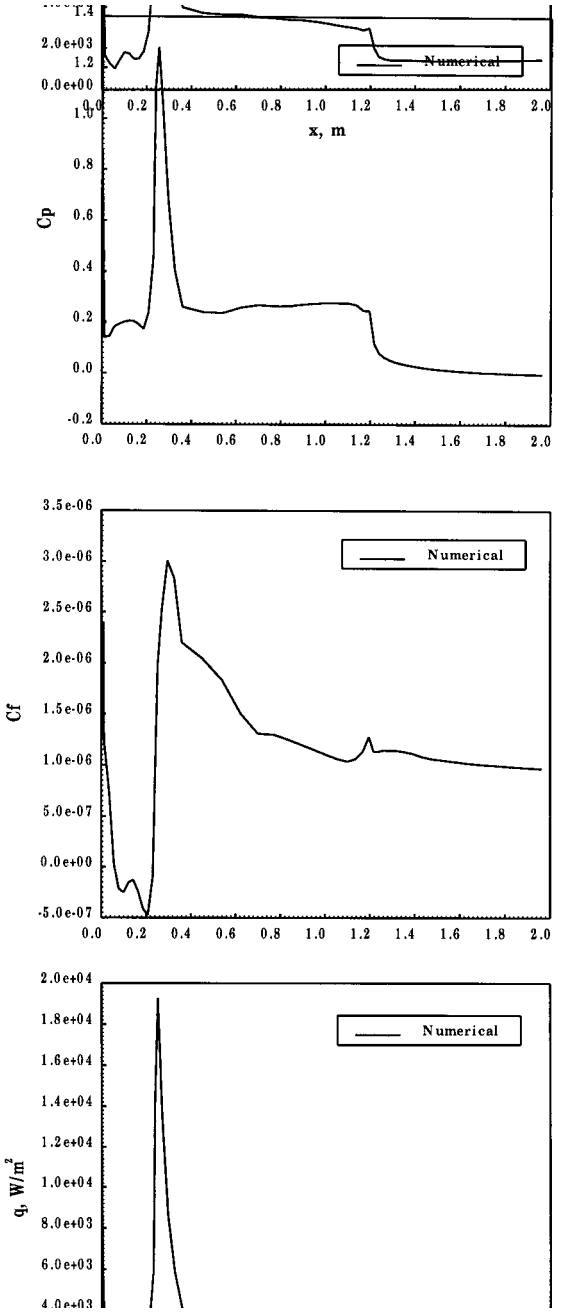

Figure 13.
Distribution of surface pressure coefficient, skin friction coefficient and wall heat flux at $M_\infty = 4.5$

References

Alonse, J., Martinelli, L. and Jameson, A. (1995), "Multigrid unsteady Navier-Stokes calculations with aeroelastic applications", AIAA paper 95-0048.

Bogdonoff, S.M. and Vas, I.E. (1958), "Preliminary investigations of spiked bodies at hypersonic speeds", Report Number 412, Dept. Aero. Engg, Princeton University, NY.

Calarese, W. and Hankey, W.L. (1985), "Modes of shock-wave oscillations on spiked-tipped bodies", *AIAA Journal*, Vol. 23 No. 2, pp. 185-92.

Chapman, D.R. (1956), "A theoretical analysis of heat transfer in region of separated flow", NACA TN 3792.

Crawford, D.H. (1959), "Investigation of the flow over a spiked nose hemisphere-cylinder at a Mach number 6.8", NASA TN-D 118.

Hoffmann, K.A. and Chiang, S.T. (1994), *Computational Fluid Dynamics for Engineers*, Vol. 2, a publication of Engineering Education System, Wichita, KS.

Jameson, A., Schmidt, W. and Turkel, E. (1981), "Numerical solution of Euler equations by finite volume methods using Runge-Kutta time stepping schemes", AIAA Paper 81-1259.

Karlovskii, V.N. and Sakharov, V.I. (1986), "Numerical investigation of supersonic flow past blunt bodies with protruding spikes", *Inv. Akad. Nauk SSSR, Mekhanika Zhidkosti i Gaza*, Vol. 3, pp. 119-27.

Mair, W.A. (1952), "Experiments on separated on boundary layers on probes in front of blunt-nosed bodies in supersonic air stream", *Philosophical Magazine*, Vol. 43, pp. 695-716.

Peyret, R. and Vivind, H. (1993), *Computational Methods for Fluid Flow*, Springer-Verlag, pp. 109-11.

Priyadarshi, P., Sivaramkrishnan, A.E. and Ganeshan, V.R. (1994), "Static pressure measurement tests on heat shield with and without angle of attack probe", Vikram Sarabhai Space Centre, Trivandrum ATTF/21/94.

Shang, J.S. (1981), "Numerical simulation of wing-fuselage interference", AIAA Paper 81-0084, January.

Shang, J.S. and Hankey, W. (1980), "Analysis of self-excited oscillations in fluid flows", AIAA Paper 80-1346.

Stalder, J.R. and Nielsen, H.V. (1954), "Heat transfer from a hemisphere-cylinder equipped with flow-separated spikes", NACA TN 3287.

Yamauchi, M., Tamura, Y., Fujii, T.Y. and Higashino, F. (1993), "Numerical investigation of supersonic flows around a spiked blunt body", AIAA Paper 93-0887.